Journal of Materials Chemistry C

ROYAL SOCIETY OF CHEMISTRY

PAPER

View Article Online
View Journal | View Issue

Cite this: J. Mater. Chem. C, 2025, 13, 5287

Voltage-control of the in-plane magnetic anisotropy in hybrid magnetoelectric $Ni_{90}Fe_{10}/BaTiO_3(011)$ heterostructures†

A. Begué, [ab] M. W. Khaliq, [c] N. Cotón, [a] M. A. Niño, [c] M. Foerster [c] and R. Ranchal *[ad]

Received 29th October 2024,
Accepted 16th January 2025

DOI: 10.1039/d4tc04614e

rsc.li/materials-c

This study focuses on hybrid magnetoelectric $Ni_{90}Fe_{10}/BaTiO_3(011)$ heterostructures, which enable the control of the in-plane magnetization of the magnetostrictive layer through electric voltage. The heterostructure is both Pb- and rare-earth-free, thus enhancing environmental sustainability. We show that the $BaTiO_3(011)$ orientation enables higher deformations in the piezoelectric regime compared to the commonly studied (001) orientation. In the as-grown state, the electrodeposited 200 nm-thick $Ni_{90}Fe_{10}$ film presents uniaxial in-plane anisotropy aligned with the [100] in-plane crystallographic direction of the $BaTiO_3(011)$ substrate. X-ray magnetic circular dichroism photoemission electron microscopy images, along with hysteresis loops obtained by the magneto-optical Kerr effect, confirm the converse magnetoelectric coupling between $Ni_{90}Fe_{10}$ and $BaTiO_3(011)$. The obtained converse magnetoelectric coupling constant of 0.205 μs m^{-1} is significant considering it is achieved in the piezoelectric regime of the $BaTiO_3$ substrate and using an electrodeposited magnetostrictive film, making this heterostructure more viable for future applications. This value represents an increase of more than double compared to that previously reported for Ni/BTO(001) and, to the best of our knowledge, is the first value reported for the BTO(011) orientation.

Introduction

Recent advancements in the manipulation of magnetic systems through electrical control have revolutionized the field, in a hot topic known as voltage control of magnetic anisotropy (VCMA).[1–5] Multiferroics stand out for their converse magnetoelectric coupling, $\alpha_E = \mu_0 \Delta M/\Delta E$, allowing an electric field (E) to change the magnetization (M).[6–8] Multiferroics can be classified into two categories: single-phase and hybrid. In single-phase multiferroics, multiple ferroic orders can coexist in the same material, *i.e.*, ferroelectricity and ferromagnetism, whereas hybrid multiferroics consist of different materials with distinct ferroic orders combined in one heterostructure to produce multiferroic behavior, *e.g.* the magnetoelectric effect. Single-phase multiferroics, such as $TbMnO_3$ with a converse magnetoelectric coupling constant of 10^{-5} μs m^{-1},[9] $Ni_3B_7O_{13}I$ with 10^{-3} μs m^{-1},[10] and Cr_2O_3 with 4.1×10^{-6} μs m^{-1},[11] have been reported. On the other hand, there are multiferroics based on hybrid systems like $BiFeO_3/BaTiO_3$, which has an α_E of 0.2 μs m^{-1},[12] NFO/PZT with 0.8 μs m^{-1},[13] and $FeRh/BaTiO_3$ with 16 μs m^{-1}.[14] Hybrid multiferroics outperform single-phase ones due to their notably higher α_E values at room temperature, while single-phase multiferroics exhibit lower or null values at room temperature.[15] Therefore, in this work, we focus on hybrid multiferroics based on strain-coupled systems, which achieve strong magnetoelectric coupling at room temperature and are ideal for applications such as memory devices, low-power logic devices, and energy harvesters.[15,16]

The mechanism of operation in these hybrid systems is the interaction between a ferroelectric substrate and a magnetostrictive layer. Applying an electric field across the ferroelectric substrate induces mechanical strain, which transfers to the magnetostrictive layer. This strain modifies the magnetic anisotropy of the top layer through inverse magnetostriction. To improve control over the magnetic anisotropy, it is crucial to use ferroelectrics with high piezoelectric coefficients and ferromagnets with both low anisotropy and large magnetostriction.[5] Typical ferroelectrics used in strain-coupled systems are based on Pb, such as PZT[17,18] and PMN-PT,[19–23] due to their

[a] Dpto. Física de Materiales, Fac. CC. Físicas. Universidad Complutense de Madrid, Plaza de las Ciencias 1, Madrid 28040, Spain. E-mail: rociran@ucm.es
[b] Fac. Ciencias. Universidad de Zaragoza, C. de Menéndez Pelayo 24, Zaragoza 50009, Spain
[c] ALBA Synchrotron Light Facility, Carrer de la llum 2-26, Cerdanyola del Vallès 08290, Spain
[d] Instituto de Magnetismo Aplicado, UCM-ADIF-CSIC, Las Rozas 28232, Spain

† Electronic supplementary information (ESI) available. See DOI: https://doi.org/10.1039/d4tc04614e

ability to achieve high strain with low voltage. For ferromagnets, the highest magnetostriction can be achieved by using rare-earth ferromagnets like Terfenol or Terfenol-D.[24] In this work, we aim to develop an environmentally friendly heterostructure capable of controlling magnetic anisotropy without relying on Pb or rare-earth elements.

Magnetostrictive ferromagnets, particularly Ni_xFe_{100-x} alloys, have been shown to be effective in VCMA systems.[5] Previously, we demonstrated control of the magnetic anisotropy of electrodeposited Ni_xFe_{100-x} alloys by means of growth parameters such as stirring, applied magnetic field during deposition, film thickness, or alloy composition.[25–27] The $Ni_{90}Fe_{10}$ composition exhibits a negative magnetostriction of −22 ppm, and in particular, a 200 nm thick film shows an in-plane (IP) isotropic magnetic behavior,[25] which is compatible with strain-induced systems due to its absence of IP anisotropy and low coercivity. This layer thickness, 200 nm, is chosen to avoid charge-mediated effects that cause magnetoelectric coupling at the ferroelectric/ferromagnetic interface. As reported by Zhou and collaborators in ref. 28, they calculated that the charge-mediated effect decays beyond 1.2 nm and later experimentally showed in ref. 29 that for a 50 nm film the effect is negligible. Similarly, Paudel *et al.*[30] reported a comparable result, measured by polarized neutron reflectometry, showing that the effect extends to only 2 nm. On the other hand, strain is a volumetric effect that affects all the upper layers if they are thinner than the substrate.[30,31] Thus, a 200 nm NiFe layer is sufficiently thick to eliminate charge-mediated effects, and the primary mechanism governing the magnetoelectric coupling will be the strain-coupling mechanism.

$BaTiO_3$ (BTO), a well-studied ferroelectric material with a perovskite-like structure,[32] is a viable substrate for strain-coupled systems. It can generate strain through three main mechanisms: photostriction,[33–35] and thermal[36–38] or voltage induction.[39–41] We specifically investigated voltage induction among these three possibilities, as it enables operation at room temperature and device integration. Although BTO is ferroelectric, in this work, we exploit its piezoelectric regime because it allows for operation at several frequencies and it is independent of polarization switching, leading to a longer lifespan for future applications.[42] This is advantageous because polarization switching can be challenging,[19] and ferroelectric materials may fatigue after many cycles, leading to unreliable performance.[43] The lifespan of a perovskite that switches its polarization is around 10^4 cycles before experiencing fatigue,[44] while in the piezoelectric regime, it can withstand fatigue after 10^8 cycles.[45] The BTO(011) surface has been scarcely explored in the context of strain-coupled systems. However, this BTO cut takes advantage of the piezoelectric coefficient d_{15}, which is one order of magnitude larger than the other coefficients. Therefore, the use of d_{15} can potentially increase the capability of BTO(011) for VCMA, as it is shown in this work in which α_E = 0.205 μs m^{-1} is obtained. In previous studies exploiting other BTO orientations in which the switching of the polarization is needed, α_E of 0.1–0.2 μs m^{-1} was reported.[46–48]

Experimental section

We have used a single-crystal BTO(011) substrate onto which a metallic Ti/Au bilayer was deposited on both sides using an e-beam evaporator under high vacuum conditions. The bottom metallic bilayer serves as an electrode for voltage application, while the top bilayer provides the necessary electrical conductivity for electrodeposition, given the non-conductive nature of BTO. Electrical isolation between both sides creates a plane-parallel capacitor around the substrate. On the polished side of the BTO, a 200 nm-thick $Ni_{90}Fe_{10}$ layer was electrodeposited over the conductive Ti/Au bilayer. Therefore, the hybrid magnetoelectric heterostructure consists of Au(50 nm)/Ti(15 nm)/BTO(500 μm)/Ti(15 nm)/Au(50 nm)/$Ni_{90}Fe_{10}$(200 nm) as illustrated in Fig. 1a where the electric voltage applied during measurements is also indicated. Electrodeposition was conducted using a PalmSens EmStat3 setup in a controlled environment with a three-electrode cell configuration at room temperature. The top Au capping layer served as the working electrode, a platinum mesh as the counter electrode, and

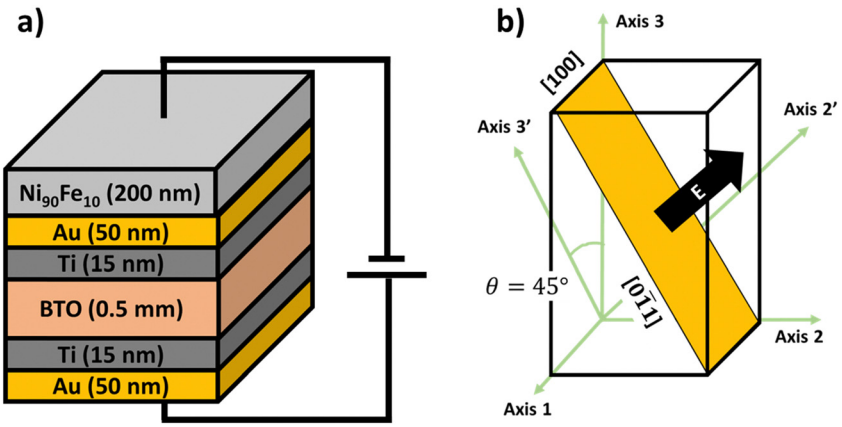

Fig. 1 (a) Schematic drawing of the studied heterostructure showing the applied electric voltage. (b) BTO(011) surface (yellow) showing the IP directions, [100] and [0$\bar{1}$1], and the electric field applied in the OOP direction for the BTO(011) orientation studied in this work. The green axes represent the coordinate axes for the piezoelectric matrix. Axes 2′ and 3′ are obtained after a rotation of θ = 45° around axis 1.

Ag/AgCl (3 M NaCl) as the reference electrode. The electrolyte, a water-based solution with a pH of 2.4, consisted of 0.4 M H_3BO_3, 0.017 M saccharine, 0.7 M $NiSO_4$, and 0.02 M $FeSO_4$. A growth voltage of −1.20 V was applied, and film thickness was monitored by measuring the electric charge at the working electrode. Film composition was analyzed using energy dispersive X-ray spectroscopy (EDS) with a JEOL JSM 6400 instrument operating at 15 kV acceleration voltage.

We studied the room temperature magneto-optic Kerr effect (MOKE) in the longitudinal configuration using s-polarized light. Our home-made experimental setup includes a laser operating at 650 nm with a power output of 5 mW and a frequency of 10 kHz, along with two polarizers, a photodetector, and an electromagnet capable of generating a magnetic field of up to 600 mT. The applied magnetic field is continuously monitored using a Hall probe. The signal detected by the photodetector is processed by a lock-in amplifier model SR830m. To apply an electric field perpendicular to the sample during MOKE measurements, a custom holder was designed and connected to a voltage power supply capable of applying 600 V. The voltage was continuously applied during the *in situ* MOKE measurements to ensure that the hysteresis loops were recorded in a sequential manner. Data acquisition was carried out using a custom Python program.

To determine the orientation and lattice parameters of the BTO substrate, X-ray diffraction (XRD) was performed using the X'Pert PRO MRD equipment with a Cu K_α wavelength. The ESI,† includes the reciprocal space maps (RSMs) used to obtain the pristine lattice constants of BTO.

Magnetic imaging was conducted using X-ray magnetic circular dichroism photo emission electron microscopy (XMCD-PEEM) at the CIRCE beamline of the ALBA Synchrotron.[49] *In situ* electrical poling and magnetic field were applied to the sample utilizing custom-designed sample holders.[50] Magnetic images were acquired at the Fe L_3 absorption edge (∼707 eV photon energy) by imaging with low-energy secondary electrons (E_{kin} around 1–2 eV) and performing pixel-wise subtraction of images taken with left and right handed circularly polarized X-rays.

Results and discussion

The BTO(011) cut can take advantage of the remarkably high piezoelectric coefficient d_{15} = 564 pm V^{-1}.[51] This value is an order of magnitude greater than other piezoelectric coefficients, such as d_{33} = 90 pm V^{-1} and d_{31} = −33.4 pm V^{-1}.[51] For *4mm* point group crystals, the reverse piezoelectric effect can be described as follows:[52]

$$\begin{pmatrix}\varepsilon_1\\ \varepsilon_2\\ \varepsilon_3\\ \varepsilon_4\\ \varepsilon_5\\ \varepsilon_6\end{pmatrix} = \begin{pmatrix}0 & 0 & d_{31}\\ 0 & 0 & d_{31}\\ 0 & 0 & d_{33}\\ 0 & d_{15} & 0\\ d_{15} & 0 & 0\\ 0 & 0 & 0\end{pmatrix}\begin{pmatrix}E_1\\ E_2\\ E_3\end{pmatrix} = \begin{pmatrix}d_{31}E_3\\ d_{31}E_3\\ d_{33}E_3\\ d_{15}E_2\\ d_{15}E_1\\ 0\end{pmatrix} \quad (1)$$

where ε_i are the strain components, d_i the piezoelectric coefficients, and E_i the applied electric field components. The *c*-axis of BTO is chosen, as usual, as axis 3 (Fig. 1b). When an out-of-plane (OOP) electric field is applied to the BTO(011) surface, the unit electric vector aligns with the surface, resulting in $\hat{E}$ = (0, 1, 1). From Eqn 1 it is obtained that $\varepsilon_4 = d_{15}E_2$, indicating a strain component proportional to d_{15}. As the BTO(011) surface is not aligned with the main axes (*i.e.*, 1, 2, and 3), shear stress components (*i.e.*, 4, 5, and 6) are transferred to the surface. This behavior is particularly significant for BTO(011), where shear components related to d_{15} will play a crucial role in the surface strain. When compared with the generally studied BTO(001) orientation, it becomes evident that for this orientation, there are no strain components dependent on d_{15} ($E_1 = E_2 = 0$) in the piezoelectric regime. This difference highlights the potential of the BTO(011) orientation compared to the (001) orientation to achieve large strain and, consequently, a higher α_E.

To calculate the dependence of the IP strain on the piezoelectric coefficients for BTO(011), we consider $a \sim c$. The OOP electric field is given by $\vec{E} = (E_1, E_2, E_3) = \frac{1}{\sqrt{2}}E(0, 1, 1)$, to satisfy that $|\vec{E}| = E$. Fig. 1b shows the coordinate axes of our system (green), where it is straightforward to see that the strain along the BTO[100] axis is equal to the strain along axis 1. To calculate the strain along the BTO[0$\bar{1}$1] direction, we need to rotate the coordinate axes around axis 1 by an angle θ to achieve the new axes 2′ and 3′, where 3′ is along the [0$\bar{1}$1] direction. As we consider that $a \sim c$, the angle of rotation will be $\theta = 45^\circ$. The strain along axis 3′ can be calculated using the following equation:[53]

$$\varepsilon_3' = \varepsilon_3 \cos^2\theta + \varepsilon_2 \sin^2\theta + \varepsilon_4 \sin\theta\cos\theta = \frac{1}{2}(\varepsilon_3 + \varepsilon_2 + \varepsilon_4) \quad (2)$$

Taking into account the results from eqn (1), we finally have that:

$$\varepsilon_{[100]} = \varepsilon_1 = \frac{1}{\sqrt{2}}Ed_{31} \simeq -24 \times 10^{-12} \cdot E \quad (3)$$

$$\varepsilon_{[0\bar{1}1]} = \varepsilon_3' = \frac{1}{2\sqrt{2}}E(d_{31} + d_{33} + d_{15}) \simeq 220 \times 10^{-12} \cdot E \quad (4)$$

The comparison between eqn (3) and (4) shows that the strain along the [0$\bar{1}$1] direction will be an order of magnitude higher than that along the [100] direction. Also, the signs are opposite as expected, as tension applied in one direction induces compression in the perpendicular direction to compensate for the volume change. The magnetostriction is proportional to the strain,[54] so a linear magneto-electric coupling dependence on the applied electric field is expected.

An intermediate conductive bilayer between BTO and NiFe is required for the electrodeposition of the latter on top of insulator BTO, which may affect strain transfer effectiveness. The strain transfer function depends on the thickness ratio between the layers and the substrate.[31] Since the substrate thickness is much greater than the thickness of the other layers, and assuming a rigid interface, no slipping between

layers and negligible edge effects, we can conclude that the strain is uniformly transferred from the substrate to the upper layers. However, the stress is applied differently across the layers, and we can calculate the stress transfer through the layers according to[31] as:

$$\frac{\sigma_l}{\sigma_s} = \frac{Y_l}{Y_s} \quad (5)$$

where σ_l and σ_s are the stresses, and E_l and E_s are the Young's moduli of the layer and substrate, respectively. The ratio of Young's moduli (Y_l/Y_s) determines the effectiveness of the stress transfer. Considering the Young's modulus of each material: Y_{Ti} = 115 GPa, Y_{Au} = 79 GPa, Y_{NiFe} = 96.4 GPa and Y_{BTO} = 99 GPa,[55–58] we find that the stress transfer ratios are Y_{Ti}/Y_{BTO} = 1.16, Y_{Au}/Y_{BTO} = 0.79, Y_{NiFe}/Y_{BTO} = 0.97. Note that we are using Young's modulus values from the literature, which may differ from those of our actual system due to clamping effects and/or the polycrystallinity of the layers. From the stress transfer ratios, we can infer that the stress transfer between the layers is efficient. Therefore, the introduction of intermediate metallic layers with a Young's modulus similar to BTO makes the heterostructure still viable for strain-coupling systems.

Fig. 2a presents the XRD characterization of pristine BTO(011). θ–2θ diffraction patterns confirmed that the BTO surface corresponds to either the (011) or (101) orientations. Through additional RSM measurements, we determined that the surface of the studied BTO is (011), with IP directions [0$\bar{1}$1] and [100], and lattice parameters: a_0 = 3.994 Å and c_0 = 4.034 Å (Fig. 2b and ESI†). Fig. 2c shows the IP MOKE hysteresis loops for the as-grown $Ni_{90}Fe_{10}$, revealing a clear IP uniaxial anisotropy aligned with the BTO [100] direction. Electrodeposited layers on glass substrates of the same thickness are magnetically isotropic in the sample plane.[27] However, the appearance of this uniaxial IP anisotropy indicates that this BTO orientation highly influences the magnetic behavior of $Ni_{90}Fe_{10}$, as the easy magnetic axis aligns with the short side of the rectangular BTO cell on the surface.

After characterizing the as-grown state, we applied electric fields of ±0.46 MV m^{-1} to pole the sample at the CIRCE beamline. These electric field values are below the ferroelectric coercive field of BTO (0.60 MV m^{-1}),[59] ensuring that the experiment was carried out within the piezoelectric regime. Fig. 3a shows XMCD-PEEM images, and Fig. 3b is a schematic illustration to interpret those results. Whereas for E = −0.46 MV m^{-1}, XMCD-PEEM shows minimal contrast, for E = +0.46 MV m^{-1}, the image displays a clear contrast that reveals IP uniaxial magnetic anisotropy (red arrows indicate the magnetization vectors). These experimental results can be understood thanks to Fig. 3b that depicts the BTO cell with blue arrows for the direction of mechanical stress promoted by poling. For negative bias (left panel), the IP strain tends to make the cell squarer, diminishing the magnetic anisotropy of

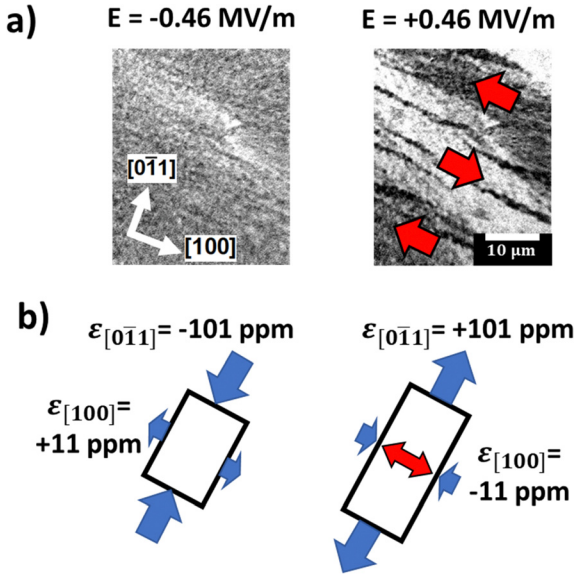

Fig. 3 (a) XMCD-PEEM images taken at E = ±0.46 MV m^{-1} with the same scale bar. IP axes (white) as well as the magnetization (red) are indicated. (b) Schematic drawings illustrate how the stress (blue arrows) generated by poling changes the size of the piezoelectric substrate that induces a modification of the magnetization on the magnetostrictive layer (red arrow) as a result. The left panel shows the interpretation of the XMCD-PEEM image at E = −0.46 MV m^{-1}, and the right panel at E = +0.46 MV m^{-1}.

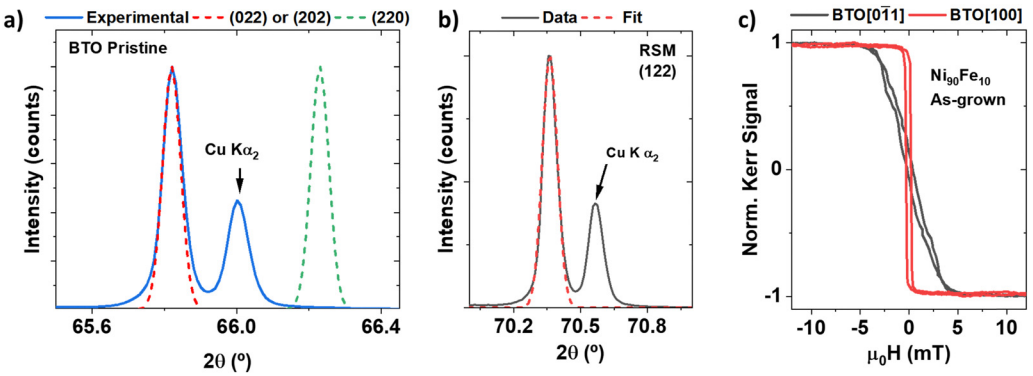

Fig. 2 (a) θ–2θ XRD measurements of pristine BTO(011) (blue line) compared with possible surface orientations (red and green dashed lines). (b) RSM measurement (black line) of the (122) reflection and corresponding fit (red dashed line). (c) MOKE hysteresis loops of as-grown $Ni_{90}Fe_{10}$ layer along IP hard and easy directions, corresponding to in-plane BTO [0$\bar{1}$1] (black line) and [100] directions (red line), respectively.

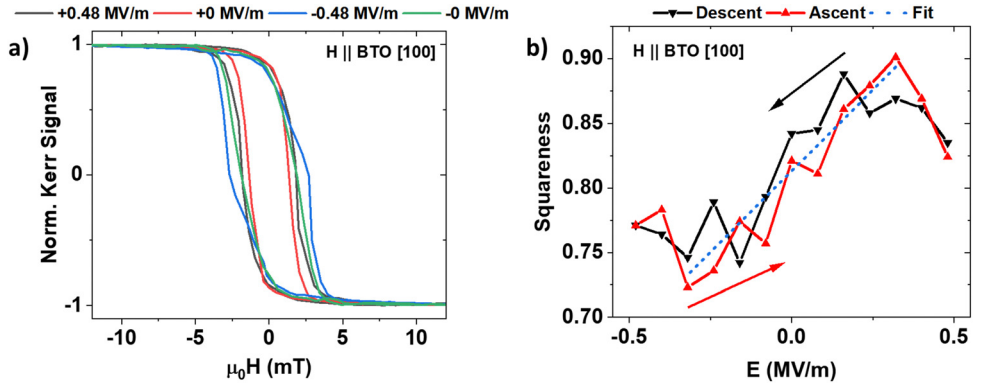

Fig. 4 (a) IP MOKE hysteresis loops for $Ni_{90}Fe_{10}$ taken along the BTO [100] direction at several polings. (b) Squareness (M_r/M_s) represented as a function of poling. Descent (black down triangles) and ascent (red up triangles) electric paths are shown differently for clarity. The linear fit of $\frac{\Delta(M_r/M_s)}{\Delta E}$ is used to obtain α_E according to eqn (6) of the main text.

the magnetostrictive $Ni_{90}Fe_{10}$. On the other hand, for positive bias (right panel) it elongates the cell in the $[0\bar{1}1]$ direction, enhancing the uniaxial magnetic anisotropy in the [100] direction according to the negative magnetostriction of $Ni_{90}Fe_{10}$.

MOKE hysteresis loops with the applied magnetic field along the BTO [100] direction were conducted under several applied electric fields between ± 0.46 MV m^{-1} to quantify α_E for the $Ni_{90}Fe_{10}$/BTO(011) heterostructure. Fig. 4a presents a representative set of IP hysteresis loops at four different applied electric fields. Here, +0 MV m^{-1} is used for zero electric field after a positive bias, while -0 MV m^{-1} denotes zero electric field after a negative bias. By calculating the squareness (M_r/M_s) for each cycle, we can plot its value at different electric fields, as depicted in Fig. 4b. The higher squareness for positive bias indicates a better alignment of the easy axis in the studied direction, whereas the reduction of the squareness for negative bias points to a loss of magnetization alignment or a reduction in magnetic anisotropy, as observed by XMCD-PEEM in Fig. 3a.

The observed behavior indicates a linear coupling between magnetism and the electric field, as expected. From the linear fit of the squareness as a function of the applied electric field (Fig. 4b), α_E is obtained as:

$$\alpha_E = \mu_0 M_s \frac{\Delta(M_r/M_s)}{\Delta E} \quad (6)$$

where μ_0 is the vacuum permeability, and M_s is the saturation magnetization of $Ni_{90}Fe_{10}$, which is 652 kA m^{-1}.[54] From the linear fit it is obtained $\alpha_E = 0.205$ μs m^{-1} = 61.5 mV (cm Oe)$^{-1}$ that can be compared with other works performed with the BTO(001) orientation. Researchers found α_E for strain-coupled heterostructures to be 0.09 μs m^{-1} for Ni/BTO,[46] 0.1 μs m^{-1} for Fe_3O_4/BTO,[47] 0.23 μs m^{-1} for $La_{0.67}Sr_{0.33}MnO_3$/BTO[48] and 16 μs m^{-1} for FeRh/BTO.[14] In these cases, the differences in α_E arise from the magnetostrictive layer, with the highest values associated with rare-earth alloys. In our study, the $Ni_{90}Fe_{10}$ alloy exhibits a magnetostriction of -22 ppm,[25] which is comparable to that of Fe_3O_4 (-25 ppm)[60] and even to pure Ni (-37 ppm).[54] Comparing our α_E value is noteworthy, as we achieved a value that is nearly double that of previous studies, demonstrating the enhanced performance of our heterostructure.

Conclusions

In conclusion, this study offers valuable insights into the Pb- and rare-earth-free $Ni_{90}Fe_{10}$/BTO(011) strain-mediated heterostructures, demonstrating their capability to control magnetic anisotropy through an electric field. The as-grown $Ni_{90}Fe_{10}$ film exhibits uniaxial IP anisotropy promoted during growth by the BTO(011) substrate. By poling the sample within the piezoelectric regime, it is possible to tune this IP magnetic anisotropy, as observed in XMCD-PEEM images. MOKE hysteresis loops measured at various polings demonstrated a noteworthy converse magnetoelectric coefficient of $\alpha_E = 0.205$ μs m^{-1}. The α_E value in our work is more than double the previously reported value for Fe_3O_4/BTO(001) (which has a similar magnetostriction layer) and, to the best of our knowledge, is the first value reported for the BTO(011) orientation. Future research could focus on using deposition systems that can deposit directly onto the substrate, eliminating the need for intermediate layers. This could improve stress transfer from the substrate to the layer, increasing the magnetoelectric coupling value, and broadening its applications in efficient magnetic memories.

Author contributions

The manuscript was written through contributions from all authors. All authors have given approval to the final version of the manuscript. A. Begué: data curation (lead); analysis (lead); investigation (lead); methodology; writing – original draft (lead). M. W. Khaliq: investigation; methodology. N. Cotón: investigation; methodology. M. A. Niño: analysis; investigation; methodology; funding acquisition; writing – review & editing. M. Foerster: analysis; investigation; methodology; funding acquisition; writing – review & editing. R. Ranchal: data curation; analysis; investigation; methodology (lead); conceptualization (lead); funding acquisition; project administration; writing – review & editing.

Data availability

The data that support the findings of this study are available from the corresponding author upon reasonable request.

Conflicts of interest

The authors have no conflicts to disclose.

Acknowledgements

This work has been financially supported through the projects PID2021-122980OB-C51 (AEI/FEDER) and PID2021-122980OB-C54 (AEI/FEDER) of the Spanish Ministry of Science and Innovation. A. B. would like to acknowledge the funding received from the Ministry of Universities and the European Union-Next Generation for the Margarita Salas fellowship. These experiments were performed on the BL24-CIRCE beamline at the ALBA Synchrotron with the collaboration of ALBA staff. We thank the CAI X-ray Diffraction Unit and Ion Implantation Unit at the Complutense University of Madrid for their valuable technical assistance.

References

1 K. Cai, M. Yang, H. Ju, S. Wang, Y. Ji, B. Li, K. W. Edmonds, Y. Sheng, B. Zhang, N. Zhang, S. Liu, H. Zheng and K. Wang, Electric field control of deterministic current-induced magnetization switching in a hybrid ferromagnetic/ferroelectric structure, *Nat. Mater.*, 2017, **16**, 712–716.

2 H. Meer, F. Schreiber, C. Schmitt, R. Ramos, E. Saitoh, O. Gomonay, J. Sinova, L. Baldrati and M. Kläui, Direct Imaging of Current-Induced Antiferromagnetic Switching Revealing a Pure Thermomagnetoelastic Switching Mechanism in NiO, *Nano Lett.*, 2020, **21**, 114–119.

3 P. Wadley, B. Howells, J. Železný, C. Andrews, V. Hills, R. P. Campion, V. Novák, K. Olejník, F. Maccherozzi, S. S. Dhesi, S. Y. Martin, T. Wagner, J. Wunderlich, F. Freimuth, Y. Mokrousov, J. Kuneš, J. S. Chauhan, M. J. Grzybowski, A. W. Rushforth, K. W. Edmonds, B. L. Gallagher and T. Jungwirth, Electrical switching of an antiferromagnet, *Science*, 2016, **351**, 587–590.

4 T. Koyama, Y. Nakatani, J. Ieda and D. Chiba, Electric field control of magnetic domain wall motion *via* modulation of the Dzyaloshinskii-Moriya interaction, *Sci. Adv.*, 2018, **4**, 0265.

5 C. Song, B. Cui, F. Li, X. Zhou and F. Pan, Recent progress in voltage control of magnetism: Materials, mechanisms, and performance, *Prog. Mater. Sci.*, 2017, **87**, 33–82.

6 K. F. Wang, J.-M. Liu and Z. F. Ren, Multiferroicity: the coupling between magnetic and polarization orders, *Adv. Phys.*, 2009, **58**, 321–448.

7 N. A. Spaldin and R. Ramesh, Advances in magnetoelectric multiferroics, *Nat. Mater.*, 2019, **18**, 203–212.

8 C. N. R. Rao and C. R. Serrao, New routes to multiferroics, *J. Mater. Chem.*, 2007, **17**(47), 4931–4938.

9 N. Hur, S. Park, P. A. Sharma, J. S. Ahn, S. Guha and S.-W. Cheong, Electric polarization reversal and memory in a multiferroic material induced by magnetic fields, *Nature*, 2004, **429**, 392–395.

10 E. Ascher, H. Rieder, H. Schmid and H. Stössel, Some Properties of Ferromagnetoelectric Nickel-Iodine Boracite, Ni3B7O13I, *J. Appl. Phys.*, 1966, **37**, 1404–1405.

11 V. J. Folen, G. T. Rado and E. W. Stalder, Anisotropy of the Magnetoelectric Effect in Cr_2O_3, *Phys. Rev. Lett.*, 1961, **6**, 607–608.

12 R. Gupta, S. Chaudhary and R. K. Kotnala, Interfacial Charge Induced Magnetoelectric Coupling at $BiFeO_3/BaTiO_3$ Bilayer Interface, *ACS Appl. Mater. Interfaces*, 2015, **7**, 8472–8479.

13 Z. Zheng, P. Zhou, Y. Liu, K. Liang, R. G. Tanguturi, H. Chen, G. Srinivasan, Y. Qi and T. Zhang, Strain effect on magnetoelectric coupling of epitaxial NFO/PZT heterostructure, *J. Alloys Compd.*, 2020, **818**, 152871.

14 R. O. Cherifi, V. Ivanovskaya, L. C. Phillips, A. Zobelli, I. C. Infante, E. Jacquet, V. Garcia, S. Fusil, P. R. Briddon, N. Guiblin, A. Mougin, A. A. Ünal, F. Kronast, S. Valencia, B. Dkhil, A. Barthélémy and M. Bibes, Electric-field control of magnetic order above room temperature, *Nat. Mater.*, 2014, **13**, 345–351.

15 R. Gupta and R. K. Kotnala, A review on current status and mechanisms of room-temperature magnetoelectric coupling in multiferroics for device applications, *J. Mater. Sci.*, 2022, **57**, 12710–12737.

16 A. Nicolenco, A. Gómez, X.-Z. Chen, E. Menéndez, J. Fornell, S. Pané, E. Pellicer and J. Sort, Strain gradient mediated magnetoelectricity in Fe-Ga/P(VDF-TrFE) multiferroic bilayers integrated on silicon, *Appl. Mater. Today*, 2020, **19**, 100579.

17 J. Ryu, S. Priya, K. Uchino and H.-E. Kim, Magnetoelectric Effect in Composites of Magnetostrictive and Piezoelectric Materials, *J. Electroceram.*, 2002, **8**, 107–119.

18 S.-K. Kim, J.-W. Lee, S.-C. Shin, H. W. Song, C. H. Lee and K. No, Voltage control of a magnetization easy axis in piezoelectric/ferromagnetic hybrid films, *J. Magn. Magn. Mater.*, 2003, **267**, 127–132.

19 A. Begué and M. Ciria, Strain-Mediated Giant Magnetoelectric Coupling in a Crystalline Multiferroic Heterostructure, *ACS Appl. Mater. Interfaces*, 2021, **13**, 6778–6784.

20 L. Leiva, J. L. Ampuero Torres, J. E. Gómez, D. Velázquez Rodriguez, J. Milano and A. Butera, Electric field control of magnetism in FePt/PMN-PT heterostructures, *J. Magn. Magn. Mater.*, 2022, **544**, 168619.

21 A. Chen, H.-G. Piao, C. Zhang, X.-P. Ma, H. Algaidi, Y. Ma, Y. Li, D. Zheng, Z. Qiu and X.-X. Zhang, Switching magnetic strip orientation using electric fields, *Mater. Horiz.*, 2023, **10**, 3034–3043.

22 M. Buzzi, R. V. Chopdekar, J. L. Hockel, A. Bur, T. Wu, N. Pilet, P. Warnicke, G. P. Carman, L. J. Heyderman and F. Nolting, Single Domain Spin Manipulation by Electric Fields in Strain Coupled Artificial Multiferroic Nanostructures, *Phys. Rev. Lett.*, 2013, **111**, 027204.

23 S. Finizio, M. Foerster, M. Buzzi, B. Krüger, M. Jourdan, C. A. F. Vaz, J. Hockel, T. Miyawaki, A. Tkach, S. Valencia, F. Kronast, G. P. Carman, F. Nolting and M. Kläui, Magnetic

Anisotropy Engineering in Thin Film Ni Nanostructures by Magnetoelastic Coupling, *Phys. Rev. Appl.*, 2014, **1**, 021001.
24 R. Grössinger, R. S. Turtelli and N. Mehmood, *Materials with high magnetostriction*, IOP Conference Series: Materials Science and Engineering, 2014, vol. 60, p. 012002.
25 N. Cotón, J. P. Andrés, E. Molina, M. Jaafar and R. Ranchal, Stripe domains in electrodeposited $Ni_{90}Fe_{10}$ thin films, *J. Magn. Magn. Mater.*, 2023, **565**, 170246.
26 N. Cotón, J. P. Andrés, M. Jaafar, A. Begué and R. Ranchal, Tuning the out-of-plane magnetic textures of electrodeposited $Ni_{90}Fe_{10}$ thin films, *J. Appl. Phys.*, 2024, **135**, 093905.
27 A. Begué, N. Cotón and R. Ranchal, Magnetic anisotropy evolution with Fe content in electrodeposited $Ni_{100-x}Fe_x$ thin films, *J. Mater. Chem. C*, 2024, **12**, 10104–10109.
28 Z. Zhou, T. X. Nan, Y. Gao, X. Yang, S. Beguhn, M. Li, Y. Lu, J. L. Wang, M. Liu, K. Mahalingam, B. M. Howe, G. J. Brown and N. X. Sun, Quantifying thickness-dependent charge mediated magnetoelectric coupling in magnetic/dielectric thin film heterostructures, *Appl. Phys. Lett.*, 2013, **103**, 232906.
29 Z. Zhou, B. M. Howe, M. Liu, T. Nan, X. Chen, K. Mahalingam, N. X. Sun and G. J. Brown, Interfacial charge-mediated non-volatile magnetoelectric coupling in Co0.3Fe0.7/Ba0.6Sr0.4TiO3/Nb:SrTiO3 multiferroic heterostructures, *Sci. Rep.*, 2015, **5**, 7740.
30 B. Paudel, I. Vasiliev, M. Hammouri, D. Karpov, A. Chen, V. Lauter and E. Fohtung, Strain vs. charge mediated magnetoelectric coupling across the magnetic oxide/ferroelectric interfaces, *RSC Adv.*, 2019, **9**, 13033–13041.
31 I. C. Noyan, T. C. Huang and B. R. York, Residual stress/strain analysis in thin films by X-ray diffraction, *Crit. Rev. Solid State Mater. Sci.*, 1995, **20**, 125–177.
32 M. Acosta, N. Novak, V. Rojas, S. Patel, R. Vaish, J. Koruza, G. A. Rossetti and J. Rödel, BaTiO3-based piezoelectrics: Fundamentals, current status, and perspectives, *Appl. Phys. Rev.*, 2017, **4**, 041305.
33 F. Rubio-Marcos, A. Del Campo, P. Marchet and J. F. Fernández, Ferroelectric domain wall motion induced by polarized light, *Nat. Commun.*, 2015, **6**, 6594.
34 F. Rubio-Marcos, D. A. Ochoa, A. Del Campo, M. A. García, G. R. Castro, J. F. Fernández and J. E. García, Reversible optical control of macroscopic polarization in ferroelectrics, *Nat. Photonics*, 2017, **12**, 29–32.
35 A. Bagri, A. Jana, G. Panchal, D. M. Phase and R. J. Choudhary, Amalgamation of Photostriction, Photodomain, and Photopolarization Effects in $BaTiO_3$ and Its Electronic Origin, *ACS Appl. Electron. Mater.*, 2022, **4**, 4438–4445.
36 M. Ghidini, F. Maccherozzi, X. Moya, L. C. Phillips, W. Yan, J. Soussi, N. Métallier, M. E. Vickers, N. Steinke, R. Mansell, C. H. W. Barnes, S. S. Dhesi and N. D. Mathur, Perpendicular Local Magnetization Under Voltage Control in Ni Films on Ferroelectric $BaTiO_3$ Substrates, *Adv. Mater.*, 2015, **27**, 1460–1465.
37 A. Bagri, A. Jana, G. Panchal, S. Chowdhury, R. Raj, M. Kumar, M. Gupta, V. R. Reddy, D. M. Phase and R. J. Choudhary, Light-Controlled Magnetoelastic Effects in Ni/$BaTiO_3$ Heterostructures, *ACS Appl. Mater. Interfaces*, 2023, **15**, 18391–18401.
38 R. V. Chopdekar and Y. Suzuki, Magnetoelectric coupling in epitaxial $CoFe_2O_4$ on $BaTiO_3$, *Appl. Phys. Lett.*, 2006, **89**, 182506.
39 S. Sahoo, S. Polisetty, C.-G. Duan, S. S. Jaswal, E. Y. Tsymbal and C. Binek, Ferroelectric control of magnetism in $BaTiO_3$ heterostructures *via* interface strain coupling, *Phys. Rev. B: Condens. Matter Mater. Phys.*, 2007, **76**, 092108.
40 Z. Q. Liu, L. Li, Z. Gai, J. D. Clarkson, S. L. Hsu, A. T. Wong, L. S. Fan, M.-W. Lin, C. M. Rouleau, T. Z. Ward, H. N. Lee, A. S. Sefat, H. M. Christen and R. Ramesh, Full Electroresistance Modulation in a Mixed-Phase Metallic Alloy, *Phys. Rev. Lett.*, 2016, **116**, 097203.
41 Y. Xie, Q. Zhan, Y. Liu, G. Dai, H. Yang, Z. Zuo, B. Chen, B. Wang, Y. Zhang, X. Rong and R.-W. Li, Electric-field control of magnetic anisotropy in $Fe_{81}Ga_{19}/BaTiO_3$ heterostructure films, *AIP Adv.*, 2014, **4**, 117113.
42 T. Li and P. S. Lee, Piezoelectric Energy Harvesting Technology: From Materials, Structures, to Applications, *Small Struct.*, 2022, **3**, 2100128.
43 A. V. Ievlev, K. C. Santosh, R. K. Vasudevan, Y. Kim, X. Lu, M. Alexe, V. R. Cooper, S. V. Kalinin and O. S. Ovchinnikova, Non-conventional mechanism of ferroelectric fatigue via cation migration, *Nat. Commun.*, 2019, **10**, 3064.
44 I. Stolichnov, A. Tagantsev, E. Colla, S. Gentil, S. Hiboux, J. Baborowski, P. Muralt and N. Setter, Downscaling of Pb(Zr,Ti)O3 film thickness for low-voltage ferroelectric capacitors: Effect of charge relaxation at the interfaces, *J. Appl. Phys.*, 2000, **88**, 2154–2156.
45 R. Salazar, M. Serrano and A. Abdelkefi, Fatigue in piezoelectric ceramic vibrational energy harvesting: A review, *Appl. Energy*, 2020, **270**, 115161.
46 T. Buttlar, T. Walther, K. Dörr and S. G. Ebbinghaus, Preparation and Magnetoelectric Behavior of Ni/$BaTiO_3$ Heterostructures with 0-3 Connectivity, *Phys. Status Solidi B*, 2020, **257**, 1900622.
47 R. Revathy, N. Kalarikkal, M. R. Varma and K. P. Surendran, Exotic magnetic properties and enhanced magnetoelectric coupling in Fe_3O_4-$BaTiO_3$ heterostructures, *J. Alloys Compd.*, 2021, **889**, 161667.
48 W. Eerenstein, M. Wiora, J. L. Prieto, J. F. Scott and N. D. Mathur, Giant sharp and persistent converse magnetoelectric effects in multiferroic epitaxial heterostructures, *Nat. Mater.*, 2007, **6**, 348–351.
49 L. Aballe, M. Foerster, E. Pellegrin, J. Nicolas and S. Ferrer, The ALBA spectroscopic LEEM-PEEM experimental station: layout and performance, *J. Synchrotron Radiat.*, 2015, **22**, 745–752.
50 M. Foerster, J. Prat, V. Massana, N. Gonzalez, A. Fontsere, B. Molas, O. Matilla, E. Pellegrin and L. Aballe, Custom sample environments at the ALBA XPEEM, *Ultramicroscopy*, 2016, **171**, 63–69.
51 M. Davis, M. Budimir, D. Damjanovic and N. Setter, Rotator and extender ferroelectrics: Importance of the shear coefficient to the piezoelectric properties of domain-engineered crystals and ceramics, *J. Appl. Phys.*, 2007, **101**, 054112.
52 A. L. Kholkin, N. A. Pertsev and A. V. Goltsev, *Piezoelectricity and Crystal Symmetry, de Piezoelectric and Acoustic Materials for Transducer Applications*, Springer, US, 2008, pp. 17–38.

53 D. Roylance, *Mechanics of materials*, Wiley, New York, 1996.
54 B. D. Cullity, *Introduction to magnetic materials*, ed. C. D. Graham, Hoboken, N. J: IEEE/Wiley, 2nd ed., 2009.
55 M. J. Donachie, *Titanium: A Technical Guide*, ASM International, Ohio, 2nd ed., 2010.
56 J. G. Noel, Review of the properties of gold material for MEMS membrane applications, *IET Circuits Dev. Syst.*, 2016, **10**, 156–161.
57 X. Li, G. Ding, T. Ando, M. Shikida and K. Sato, Micromechanical characterization of electroplated permalloy films for MEMS, *Microsyst. Technol.*, April 2007, **14**, 131–134.
58 S. Jiansirisomboon and A. Watcharapasorn, Effects of alumina nano-particulates addition on mechanical and electrical properties of barium titanate ceramics, *Curr. Appl. Phys.*, 2008, **8**, 48–52.
59 T. M. Raeder, T. S. Holstad, I.-E. Nylund, M.-A. Einarsrud, J. Glaum, D. Meier and T. Grande, Anisotropic in-plane dielectric and ferroelectric properties of tensile-strained $BaTiO_3$ films with three different crystallographic orientations, *AIP Adv.*, 2021, **11**, 025016.
60 D. Odkhuu, P. Taivansaikhan, W. S. Yun and S. C. Hong, A first-principles study of magnetostrictions of Fe_3O_4 and $CoFe_2O_4$, *J. Appl. Phys.*, 2014, **115**, 17A916.

